Cell & Bioscience

RESEARCH

Open Access

Integrating single-cell and spatial transcriptomics to reveal the spatiotemporal dynamics of retinal cells during ischemia–reperfusion injury progression in rats

Yijia Huang[1,2,3†], Junhong Guo[1,2†], Fei Yao[4†], Bingkai Feng[1,2], Di Gong[1,2], Kuanrong Dang[1,2], Tingyu Hu[2], Simin Deng[1,2], Yong Liu[1,2], Chunyan Tan[3*] and Jiantao Wang[1,2*]

Abstract

Retinal ischemia–reperfusion (I/R) injury is a key pathological process in retinal-associated diseases such as glaucoma. However, the spatiotemporal dynamics and cell interactions during this injury are not fully understood. This study integrated single-cell RNA sequencing and spatial transcriptomics to map retinal cell responses in a rat I/R injury model at acute, subacute, and chronic stages. We identified 14 cell populations and tracked gene expression changes over time. Retinal ganglion cells (RGCs) showed activation of apoptotic, autophagic, and oxidative stress pathways within 24 h. Spatial analysis revealed RGCs co-localized with Müller glial and microglial cells in the optic nerve and inner retina, with RGC death driven by ligand-receptor interactions (e.g., Ncam1-Ncam1, App-Sorl1). Transcription factors (Sox9/Sox8) in Müller cells regulated TNF/JAK-STAT signaling, while Alzheimer's-related Mapt exhibited spatiotemporal specificity in RGCs, suggesting shared neurodegenerative pathways. This study constructed a panoramic spatiotemporal dynamic map of retinal I/R injury progression, providing important clues for the development of potential therapeutic targets for glaucoma and related retinal diseases.

Keywords Retinal ischemia–reperfusion injury, Spatial transcriptome sequencing, Single-cell transcriptome sequencing, Cell and tissue heterogeneity, Glaucoma

Introduction

Retinal ischemia–reperfusion (I/R) injury is a critical pathological mechanism in the development of various retinal diseases, particularly glaucoma, which remains a leading cause of blindness globally [1]. This condition arises when the retinal blood supply is abruptly compromised and then restored, leading to an array of cellular damage, inflammation, and neuronal apoptosis [2]. Understanding the complex, dynamic responses of retinal cells during I/R injury is essential for unraveling the mechanisms behind retinal degenerative diseases and for identifying potential therapeutic targets. However,

†Yijia Huang, Junhong Guo and Fei Yao have equally contributed to this work.

*Correspondence:
Chunyan Tan
tancy@sz.tsinghua.edu.cn
Jiantao Wang
jiantaowang65@163.com
[1]Shenzhen Eye Institute of Shenzhen Eye Hospital, Jinan University, Shenzhen, Guangdong, China
[2]Shenzhen Eye Medical Center of Shenzhen Eye Hospital, Southern Medical University, Shenzhen, Guangdong, China
[3]Institute of Biopharmaceutical and Health Engineering, Tsinghua University, Shenzhen, Guangdong, China
[4]Eye Center of Xiangya Hospital, Central South University, Changsha, Hunan, China

the spatial and temporal complexity of this process, particularly in the context of retinal ganglion cell (RGC) degeneration, poses significant challenges to traditional analysis techniques. Furthermore, the current intervention treatments for retinal ischemia–reperfusion injury have achieved very limited effects (such as anti-VEGF drugs, non-steroidal anti-inflammatory drugs, and glucocorticoids) [3]. Therefore, by constructing transcriptomic profiles for multiple stages of injury, and revealing the spatiotemporal characteristics of the retinal cells, it is of crucial importance for understanding the molecular drivers of this disease and identifying potential therapeutic targets.

Although retinal ischemia–reperfusion injury can be classified into the acute phase, subacute phase and chronic phase [4, 5], the specific dynamics of retinal cell responses during the I/R injury process and the interactions between different cell populations remain unclear. While previous studies have documented the effects of I/R on specific cell types (such as RGC and Muller cells) or specific time points, the spatiotemporal organization of these responses and the interactions between various cell populations throughout the injury process have not been fully addressed [6–8]. Current methods, often limited to bulk tissue analyses, fail to capture the heterogeneous nature of retinal injury and its progression. Furthermore, the molecular pathways and cellular interactions that mediate the early apoptosis of RGCs and the subsequent retinal degeneration remain inadequately understood. This knowledge gap underscores the need for a more comprehensive approach that can simultaneously analyze gene expression, cellular localization, and their interactions in situ over time.

In recent years, advancements in transcriptomics technologies have enabled a deeper understanding of cellular states [9]. Single-cell RNA sequencing (scRNA-seq) reveals cellular heterogeneity following I/R; However, it necessitates tissue dissociation, resulting in the loss of spatial localization data, thus preventing the analysis of cell positioning within the layered structure of the retina [10]. Spatial transcriptomics (ST), in contrast, allows for the unbiased capture of transcriptomic spatial information while preserving the tissue structure [11, 12]. Although its spatial resolution is still unable to reach the single-cell level, the spatial location can provide additional information to resolve cell heterogeneity and communications in complex tissues [13]. By integrating ST and scRNA-seq technologies, key pathways and cell–cell interaction networks involved in the spatiotemporal dynamics of I/R can be systematically revealed.

For this, we chose a time course that represents different pathophysiological processes characteristic of the acute (G2h), subacute (G24h), and chronic (G7d) stages of I/R injury. By integrating spatial transcriptomics and single-cell sequencing data, we created gene expression maps of the retina and optic nerve regions. Through single-cell analysis, we identified various cell types and examined the spatial expression patterns of I/R-related genes. Furthermore, we analyzed ligand-receptor-mediated cell communication and spatiotemporal dynamic gene networks, elucidating the molecular regulatory mechanisms of I/R. Through analysis of neuron-glial cell spatial interactions, we identified key factors regulating RGC death, which involve apoptosis, senescence, oxidative stress, and autophagy pathways. We validated the spatial distribution of key genes using multi-omics in situ pairwise sequencing. This study developed a three-dimensional map of "cell type-spatial location-time dynamics," offering a comprehensive analysis of the spatiotemporal heterogeneity of I/R. This map offers novel mechanistic insights and potential therapeutic targets for I/R-related diseases, such as glaucoma.

Results

Cellular heterogeneity in the process of retinal ischemia–reperfusion injury in rats

First, we confirmed the structural and functional effects of ischemia–reperfusion(I/R) injury in the rat model (Fig. S1A, B). Histological analysis revealed that the entire retina and the retinal ganglion cell (RGC) complex progressively thinned and decreased, suggesting neuronal loss, which became particularly evident on the 7th day (Fig. S1C–G). Consistent with this, the electroretinogram showed a significant decline in retinal function, manifested by the reduction in amplitudes of the a-wave and b-wave after the injury (Fig. S2A–I). These findings confirm the successful induction of I/R injury and provide the phenotypic foundation for the subsequent molecular profiling. To explore the specific functions and mechanisms of different cell types in the retina during I/R injury, we performed single-cell RNA sequencing (scRNA-seq) on retinal tissues from a rat I/R injury model. We pooled samples from four rats (one eye per rat) at the following time points: sham (no injury), 2 h, 24 h, and 7 days after retinal I/R injury (Fig. 1A). The scRNA-seq data from the retinal tissues of the rat I/R injury model underwent stringent quality control (See Methods), resulting in a transcriptomic profile of 57,493 cells. The transcriptional expression matrix for the 57,012 cells was normalized, and principal component analysis (PCA) was performed. By selecting the top 50 principal components, dimensionality reduction and visualization were then carried out using uniform manifold approximation and projection (UMAP). Using unbiased clustering analysis, we identified 32 distinct cell clusters (Fig. S3A). Based on the characteristic gene expression of each cluster and the retinal cell-specific marker genes reported in the literature (Table S1), we identified 14

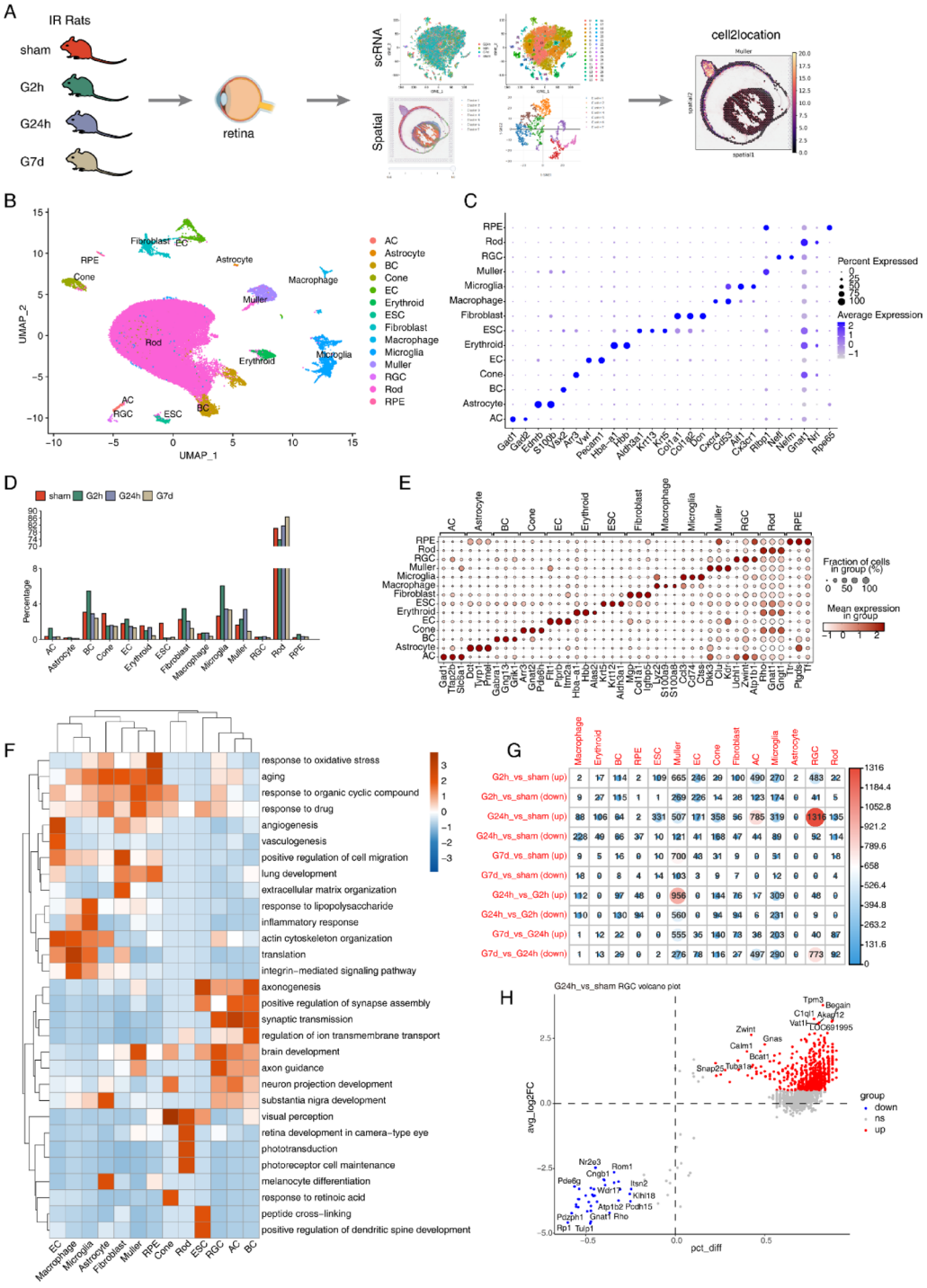

Fig. 1 (See legend on next page.)

distinct cell types, including amacrine cells (AC), astrocytes, bipolar cells (BC), cone cells, endothelial cells (EC), erythroid cells, epithelial stem cells (ESC), fibroblasts, macrophages, microglia, Müller cells, retinal ganglion cells (RGC), rod cells (Rod), and retinal pigment epithelial cells (RPE) (Fig. 1B). Consistent with previous human retinal studies, Rod are the predominant cell type [14]. We present the relative expression of marker genes used for annotating each cell type across different cell populations. The results reveal that Gnat1 was detected in several cell clusters, whereas other marker genes exhibited cell-type specific expression patterns (Figs. 1C, S3B). Next, we analyzed the composition ratios of different cell populations across the groups. The results indicate

(See figure on previous page.)

Fig. 1 Single-Cell Transcriptomic Atlas of Retinal Ischemia–Reperfusion Injury in Rats. **A** Overview of the experimental design. The process is generally divided into four steps. The first step is random grouping and model construction. The second step involves the collection and embedding of the eyeball. The third step includes library construction and sequencing of samples. The fourth step is the analysis of integrating single-cell and spatial transcriptomic data. **B** After quality filtering, normalization, dimensionality reduction, and other analyses were performed on the single-cell data using Seurat, a UMAP clustering plot was generated. Using the sctype single-cell annotation software and marker genes reported in the literature, 14 cell populations were annotated. **C** The dot plot displays the expression patterns and characteristics of the marker genes used for annotating each cell population. (The size of the dots represents the proportion of cells expressing the gene, and the color gradient from light to dark indicates a gradual increase in expression). **D** A bar chart compares the proportion of each cell population across different groups, which contain one replicate in each group. **E** The expression patterns and characteristics of the top 3 highly expressed genes in each cell type. **F** A heatmap presents the GO analysis of biological processes for the differentially expressed genes in each cell type (|log2FC|≥ 0.5 and p-value ≤ 0.05). **G** A display of the number of DEGs identified in different cell populations at various time points (*p*-value ≤ 0.05 and $|\log_2 FC| \geq 0.5$). **H** A dot plot displays the upregulated and downregulated gene results for RGC in the G24h vs. sham comparison ($|\log_2 FC| \geq 1$and *p*-value ≤ 0.05). The x-axis (Percentage Difference, Δ%) represents the difference in the percentage of cells expressing the gene (pct) between the G24h and Sham groups

that Rod dominate in all groups. Compared to the Sham group, AC, BC, and Microglia significantly increased at 2 h post-model induction, while Cone and ESC significantly decreased after modeling. Several cell types exhibited dynamic changes in their proportions. Notably, the proportions of Erythroid cells, Fibroblasts, Macrophages, and RGCs were ultimately decreased at G7d compared to the Sham group. Müller cells showed an initial increase at G2h and G24h, followed by a decline at G7d (Fig. 1D). These results indicate that I/R injury systematically alters the cellular composition of the retina, suggesting that these cells may be involved in the pathological process through modulation of their functional states. Next, we display the top three highly expressed genes in each cell population, revealing that these genes also have cell-type specific expression patterns (Fig. 1E). However, these highly expressed genes do not fully correspond to the previously identified marker genes (Fig. 1C), indicating that through scRNA-seq analysis, we have identified several potential marker genes for retinal cell types (Fig. 1E). We conducted Gene Ontology (GO) enrichment analysis on the differentially expressed genes (DEGs) for different cell populations and found that each population is predominantly enriched in pathways related to its specific cellular function. For example, Macrophages and Microglia are predominantly enriched in pathways associated with inflammation and lipopolysaccharide response; Rod and Cone cells are enriched in phototransduction-related pathways; RGCs, ACs, and BCs are jointly enriched in pathways involved in neurodevelopment, neurotransmission, and neural projection. Additionally, genes among other clusters are enriched in functional pathways associated with oxidative stress response, cellular senescence, drug response, and cell adhesion (Fig. 1F). Kyoto Encyclopedia of Genes and Genomes (KEGG) enrichment analysis revealed similar findings (Fig. S3C). These enriched pathways partly reflect the functional roles of each cell type during I/R injury and may play a role in the occurrence and progression of glaucoma. Next, we conducted DEGs analysis of gene expression across different cell types at each time point. The results indicate that the number of DEGs in different cell types is characteristic and is not simply a reflection of the total number of cells captured for that type. The G24h *vs.* Sham group showed the highest number of DEGs, while the G7d *vs.* Sham group displayed relatively fewer (Fig. 1G). This trend suggests that I/R injury has the most significant impact on cellular transcription levels within 24 h post-treatment, with a potential shift toward transcriptional recovery in the later stages. Furthermore, cell types like RGCs, ACs, Müller cells, and Microglia exhibited a higher number of DEGs. We further focused on the DEG expression characteristics of RGCs in the G24h vs. Sham group. To capture the full complexity of transcriptional changes, we plotted genes based on both their expression fold change (Log_2FC, reflecting magnitude of change in expressing cells) and their percentage difference (Δ%, reflecting change in the fraction of cells expressing the gene) (Fig. 1H). This dual-dimensional approach distinguishes between genes whose changes are driven primarily by transcriptional modulation within a stable cell subset (high Log_2FC, low Δ%) versus those driven by shifts in the expressing cell population (low Log_2FC, high Δ%). The results revealed an overall upregulation of many genes, while several key genes were downregulated, such as retinal degeneration 1 (Rpl), rhodopsin (Rho), and guanine nucleotide-binding protein alpha-transducin polypeptide 1 (Gnat1), which showed both reduced expression levels and decreased prevalence (negative Δ%), suggesting coordinated downregulation of phototransduction machinery in RGCs following injury. In conclusion, the changes in retinal cell composition induced by I/R injury may help explain the onset and progression of diseases such as glaucoma. Therefore, the changes in cell populations and enriched pathways identified in this study may encompass critical cell types and regulatory genes that play a role in the pathogenesis of glaucoma.

Spatial transcriptome profile demonstrated the localization of identified cell types

To further investigate the retinal pathology induced by I/R injury, we employed spatial transcriptomics (ST-seq) technology to examine the gene expression characteristics in retinal tissue structures and their dynamic changes

throughout the I/R injury process. Using the 10X Visium platform, with 55 μm spots that typically cover multiple cells for each, we obtained ST-seq data for the Sham group and three I/R injury time points (G2h, G24h, G7d) (Figs. 1A, S4). Specifically, each sagittal section of the eyeball, which encompasses the entire retinal structure, captured the following number of spots: 723 for the Sham group, 993 for the G2h group, 818 for the G24h group, and 998 for the G7d group. Based on the gene expression characteristics of each spatial spot, we conducted dimensionality reduction and clustering analysis for each of the four eyeball samples, similar to scRNA-seq. Using UMAP, we then performed unified dimensionality reduction and clustering analysis for all spots across the samples, identifying 11 distinct expression clusters (clustering resolution res = 0.5). The results revealed that the sixth cluster was distinctly separated from the others, while the remaining clusters exhibited relatively similar expression characteristics and grouped together (Fig. 2A). The distribution patterns of the spot clusters were fairly consistent across the four groups (Fig. 2B). Mapping the clustering results of the spots back to the retinal spatial structure revealed distinct spatial distributions for each cluster. The sixth cluster was mainly located in the optic nerve head region (Fig. S5A). Furthermore, we analyzed the proportional distribution of each cluster across different samples. The results showed substantial differences between the groups (Fig. S5B), which could be attributed to the resolution of Visium technology or the stage-specific features of retinal injury progression. Next, we integrated the scRNA-seq and ST-seq data and mapped the annotated cell types onto the spatial structure of the eyeball. Using the cell2location deconvolution analysis method [15], we analyzed the spatial distribution patterns of various cell types within the retinal structure according to the expression levels of marker genes. First, we analyzed the spatial distribution of RGCs, which were primarily localized to the inner retina and optic nerve head region (Fig. 2C). ACs and BCs are mainly localized to the inner retinal region (Fig. 2D–E), and this distribution pattern aligns with previous histopathological observations [16]. Additionally, we also show the distribution of Müller cells. Müller cells are the major glial cells in the retina, responsible for maintaining neuronal homeostasis and providing metabolic support [17]. The results indicate that the distribution of Müller cells is somewhat similar to that of RGCs, with both primarily concentrated in the inner retina and optic nerve head region (Fig. 2F). In conclusion, ST-seq data can depict the expression structure of the retina by using scRNA-seq and biomarkers, and illustrate the spatial distribution patterns of main cell types within the retina. Based on the Cell2location analysis results, we further assessed the co-localization relationships of different cell types within the same spots. The results showed that in the Sham group, RGCs co-localized with Macrophages; in the G2h group, RGCs co-localized with ACs and Erythroid cells; in the G24h group, RGCs co-localized with ACs, Macrophages, and Müller cells; and in the G7d group, RGCs primarily co-localized with ACs and Macrophages (Fig. 2G). This finding suggests that RGCs may have significant interactions with the aforementioned cell types, and that their spatial interactions demonstrate dynamic changes. Future studies will focus on the changes in the spatial distribution of different cell types under I/R injury conditions and their interaction patterns.

Dysregulated expression pattern and functional pathways of RGCs in the process of retinal I/R injury in rats

Then we analyzed the gene expression change patterns of different cell types during the I/R injury process, with a particular focus on the expression dynamics of RGCs. Using clustering analysis, we identified six distinct gene expression clusters of RGCs (Fig. 3A). Then we explored the functions of genes from Cluster 1, 2, and 4 that showed difference across the time points. Cluster 1 was primarily enriched in pathways related to RNA splicing, transcriptional regulation, protein ubiquitination, positive regulation of exogenous apoptosis signaling, and autophagy (Fig. 3B). Cluster 2 was enriched in pathways associated with protein translation, intracellular transport, oxidative stress responses, and the endogenous apoptosis signaling pathway mediated by oxidative stress (Fig. 3B). Cluster 4 was enriched in pathways related to intracellular signal transduction, protein phosphorylation, chromatin remodeling, and transcriptional regulation (Fig. 3B). Similarly, we performed expression pattern analysis on Müller cells. The results revealed that Cluster 1 was significantly upregulated in the G7d group, while Cluster 5 was notably downregulated after I/R treatment (Fig. S6A). Functional enrichment analysis revealed that Cluster 1 is mainly involved in pathways related to oxidative stress response, cellular senescence, and neuroregulation, while Cluster 5 is primarily enriched in pathways associated with visual signal transduction (Fig. S6B, C). Taken together, these results show that at the G7d stage, genes associated with apoptosis and oxidative stress pathways are significantly upregulated, whereas genes related to neuroconduction pathways are notably downregulated. This trend aligns with previous understanding of I/R injury [18]. Moreover, RGC apoptosis may be mediated through extracellular signaling pathways, with key genes including *Faf1*, *Trps1*, *Stk4*, and *Nf1*. The oxidative stress-induced endogenous apoptosis signaling pathway contained the following genes: *Gpx1*, *Arl6ip5*, *Sod2*, and *Mapt*. The autophagy-related pathway contained seven genes: *Sirt2*, *Sesn2*, *Usp10*, *Atg4c*, *Atg12*, *Atg5*, and *Vps51*. Therefore, we specifically present the

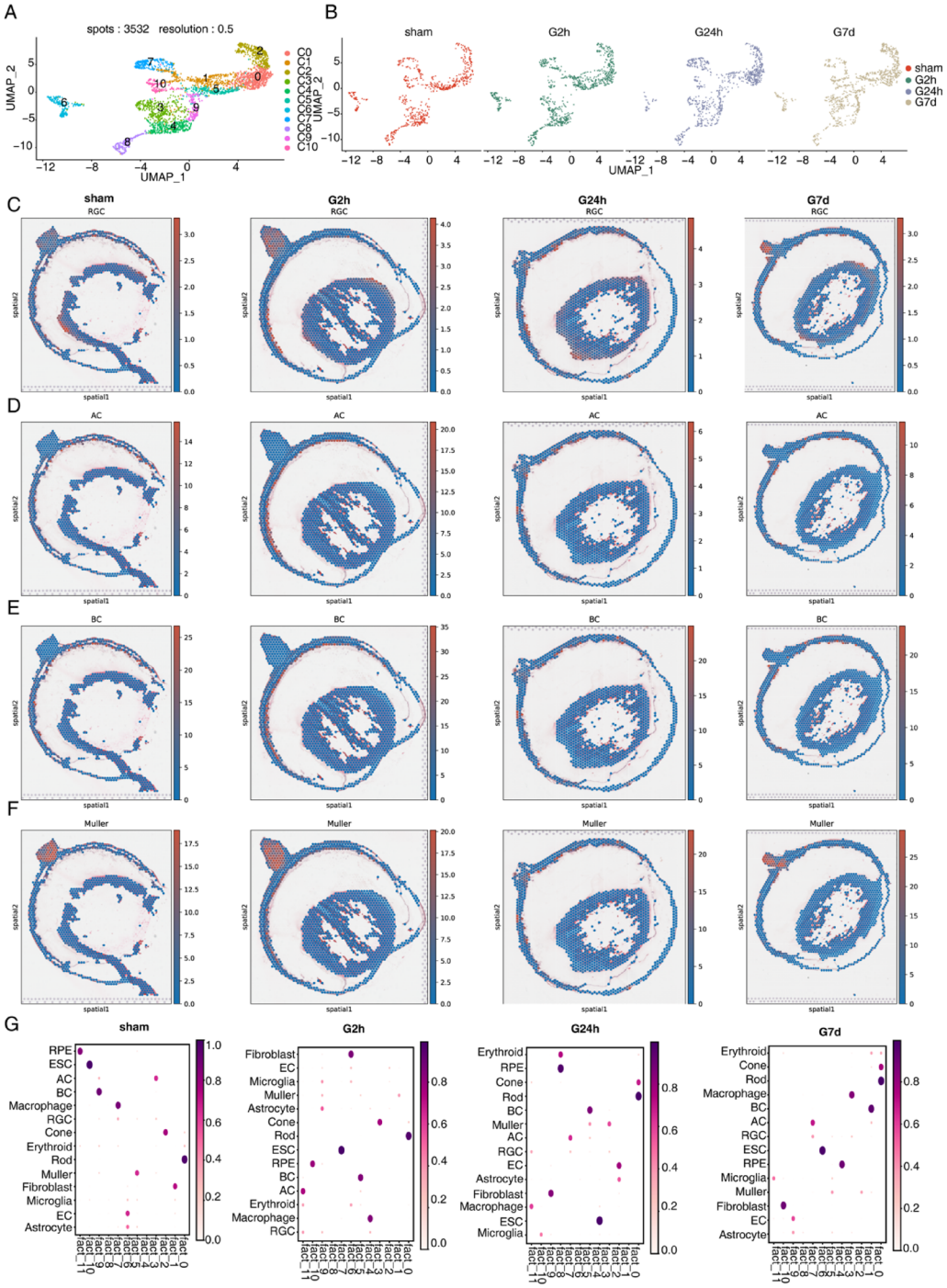

Fig. 2 Spatial Transcriptomic Atlas and Distribution Characteristics in Retinal Ischemia–Reperfusion Injury in Rats. **A** UMAP plot of the 4 samples integrated using the CCA method. **B** UMAP dimensionality reduction clustering visualization results for each of the 4 samples. **C–F** Distribution and expression characteristics of RGC, AC, BC, and Müller cells in the 4 ST-seq samples. **G** A bubble plot displaying the analysis results of cell type co-localization in the ST-seq data

expression characteristics of the aforementioned genes (Fig. 3C). Additionally, we analyzed the spatial distribution patterns of these genes in the ST-seq data. The analysis revealed that Mapt (encoding Tau protein), which is significantly associated with Alzheimer's disease [19], is predominantly expressed in the inner retina and optic nerve head region, with high spatial specificity, and is most prominently expressed in the G2h samples (Fig. 3D). Gpx1, a critical gene in the oxidative stress response [20], is highly expressed in the optic nerve head

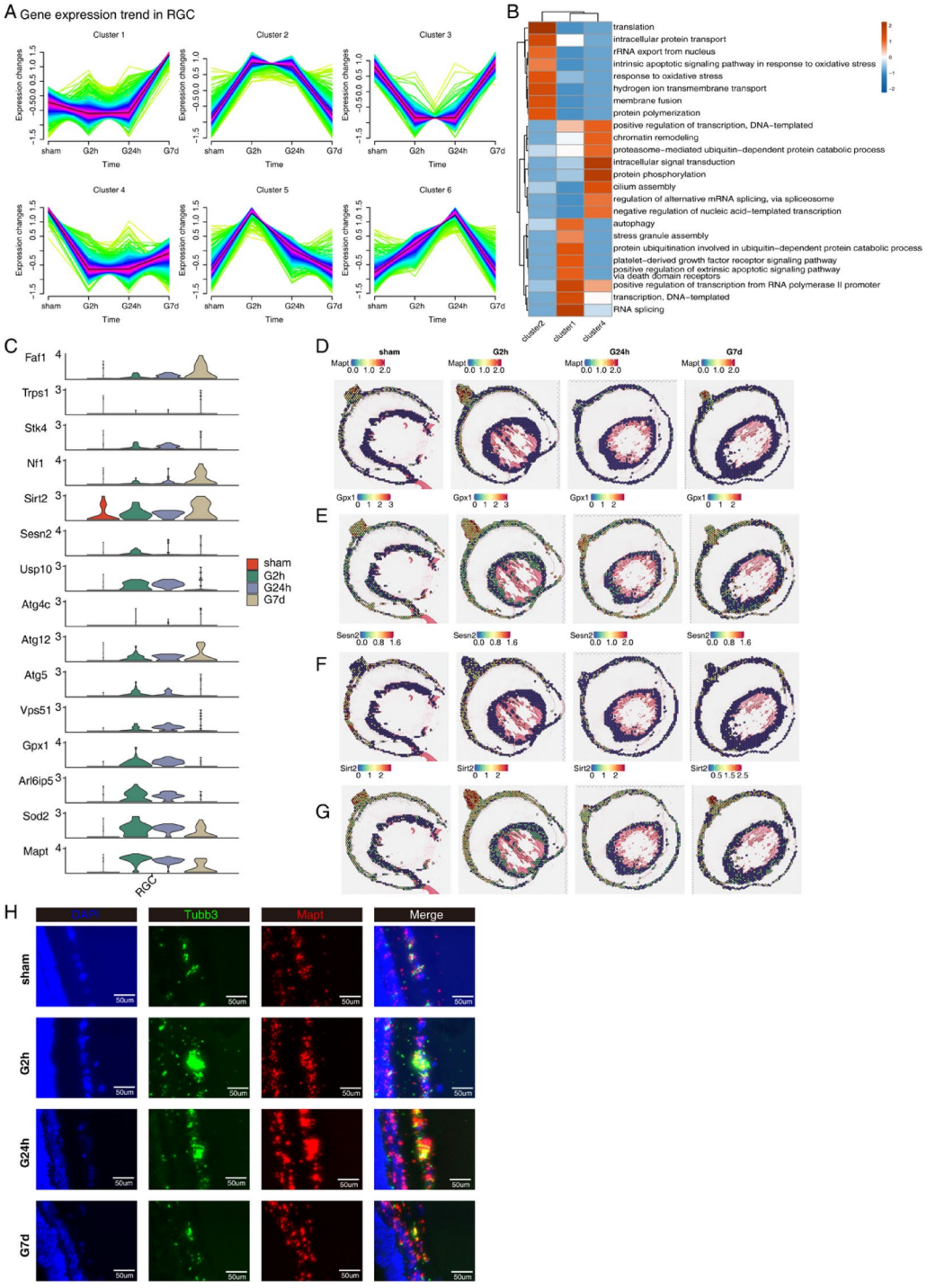

Fig. 3 Gene expression patterns and enriched functional pathways of rgc during retinal I/R injury progression. **A** Gene expression trend analysis of 6 clusters in RGC. **B** Heatmap showing the GO-BP functional pathways enriched in genes from Cluster 1, 2, and 4. **C** Violin plot showing gene expression levels associated with apoptosis, autophagy, and oxidative stress response pathways. **D–G** Displaying the spatial distribution and specific expression of the four related genes—Mapt, Gpx1, Sesn2, and Sirt2— in ST-seq. **H** MIP-seq validation of Mapt expression in RGC cells. (tubb3 marks RGC) Similar results were observed in at least three independent experiments. The scale bars in the figures are 50 μm

region after I/R injury, with its expression levels significantly elevated in the G2h and G24h samples (Fig. 3E). Sesn2 is widely expressed in the retina, with its expression gradually decreasing as the duration of I/R treatment is extended (Fig. 3F). Sirt2 is primarily localized to the optic nerve head region, with its expression gradually increasing during I/R treatment (Fig. 3G). Furthermore, MIP-seq validation confirmed that Mapt is expressed in

RGCs, with its expression showing a dynamic trend of increase followed by a decrease (Fig. 3H).In conclusion, the results show that RGCs express high levels of genes related to apoptosis, autophagy, and oxidative stress response following I/R injury. These genes demonstrate specificity both spatially and temporally, suggesting their potential involvement in regulating RGC damage.

Differential analysis of transcription factors in retinal I/R injury in rats

Transcription factors (TFs) play a crucial role in the regulation of gene transcription. Therefore, we focused on analyzing the TFs specifically expressed in each cell population, as well as the differentially expressed TFs across different time points. Given the observed dynamic changes in Müller cells and their spatial proximity to RGCs (Figs. 1D, 2F), we next investigated the transcriptional regulators driving their response to I/R injury. Based on the expression of cell population-specific TFs by the SCENIC method [21], we predicted the key regulators (regulons) and calculated their Regulon Specificity Scores (RSS). The analysis revealed that, except for Rod cells, all other cell populations exhibit specific regulons. While Rod cells express multiple specific TFs, their expression levels are generally low (Fig. 4A). The specific highly expressed TFs in different cell populations include Sox9, Sox8, Hey2, and Sox2 in Müller cells; Vsx2 and Dbp in BC cells; Mafb and Maf in Microglia; Tbx2 and Atf5 in RGCs; and Timeless in RPE cells (Fig. 4A). Müller cells are a type of glial cell extensively distributed throughout the retina, where they support retinal neurons. Dysfunction in Müller cells is closely linked to a range of retinal diseases, including glaucoma [22]. In Fig. 1, we observed that Müller cells and other cell populations (including RGCs) are enriched in aging-related functional pathways (Fig. 1F). Based on this, we specifically analyzed the differentially expressed TFs in Müller cells. The results revealed significant characteristics in both the activity strength and expression specificity of their corresponding regulons (Fig. S7A, B). Furthermore, We analyzed the expression characteristics of downstream target genes regulated by these TFs, which were identified through SCENIC's combined co-expression and motif-based filtering approach. The clustering analysis results revealed two TF clusters that were significantly upregulated in the G2h samples. We then performed functional enrichment analysis on the high-confidence target genes of these regulons (i.e., genes with both co-expression evidence and validated binding motifs), revealing predominant associations with apoptosis, TNF signaling, Jak-Stat pathways, Ras pathways, and ErbB pathways (Fig. 4B). Therefore, we focused on the TFs that regulate the above pathways and found that several factors were specifically highly expressed in Müller cells at G2h (Fig. S7C–F), suggesting that these TFs may play a crucial regulatory role during the I/R injury process. Next, we analyzed the spatial expression changes of these TFs in the retina. Crem was mainly expressed in the optic nerve head and outer retinal layers in the Sham group, but in the G2h group, its expression shifted to the inner retinal layers where it was highly expressed (Fig. 4C). Fosb was predominantly highly expressed around the optic nerve head region in the G2h and G24h groups (Fig. 4D). In addition to Fosb, Fos was also significantly highly expressed in the inner retinal layers of the G2h samples (Fig. 4E). Jun was widely expressed throughout the entire retinal region (Fig. 4F). Furthermore, we present the spatial expression distribution of Cebpb, Creb5, Maff, and Jund in the four samples (Fig. S7F). MIP-seq further confirmed that the early upregulation of TFs like Fos, Jun, and Sox9 in Müller cells, and their regulation of TNF/JAK-STAT signaling, positions Müller glia as a key signaling hub that potentially amplifies inflammatory and stress signals to neurons like RGCs, thereby mechanistically contributing to their demise (Fig. 4G).

Based on the results of the above studies, we hypothesize that transcription factors in Müller cells may play a potential regulatory role in the development of glaucoma induced by I/R injury and are closely associated with pathways such as apoptosis.

Subclusters analysis of BCs revealed their tight association with neurological and phototransduction functions

Based on the identified cell types, we observed two distinct distribution populations of BCs (Fig. 1B). To further investigate the expression characteristics of BCs, we divided the BC population into 10 cell subgroups (Fig. 5A). We then mapped these 10 cell subgroups to the two main BC distribution populations. The results revealed that subgroups 1, 3, 8, and 9 were concentrated in one population, while the other subgroups were found in the other population (Fig. 5B). This difference in expression distribution suggests that each subgroup may have functional specificity. We also analyzed the genes specifically highly expressed in each cell subgroup, finding that each subgroup has unique expression patterns and marker genes (Fig. 5C). The subgroup proportion analysis revealed that C7 significantly increased in the G7d samples, C4 increased in all I/R injury samples, while C0 and C3 showed a downward trend (Fig. 5D). Therefore, we further analyzed the functional pathway enrichment of each cell subgroup, discovering that they are mainly involved in processes such as visual signal transduction and neurotransmission (Fig. 5E). KEGG pathway enrichment analysis also revealed similar functional features (Fig. S8). Based on their congruent GO enrichment profiles, the 10 cell subgroups were classified into two categories: subgroups 1, 3, 4, 8, and 9 form one

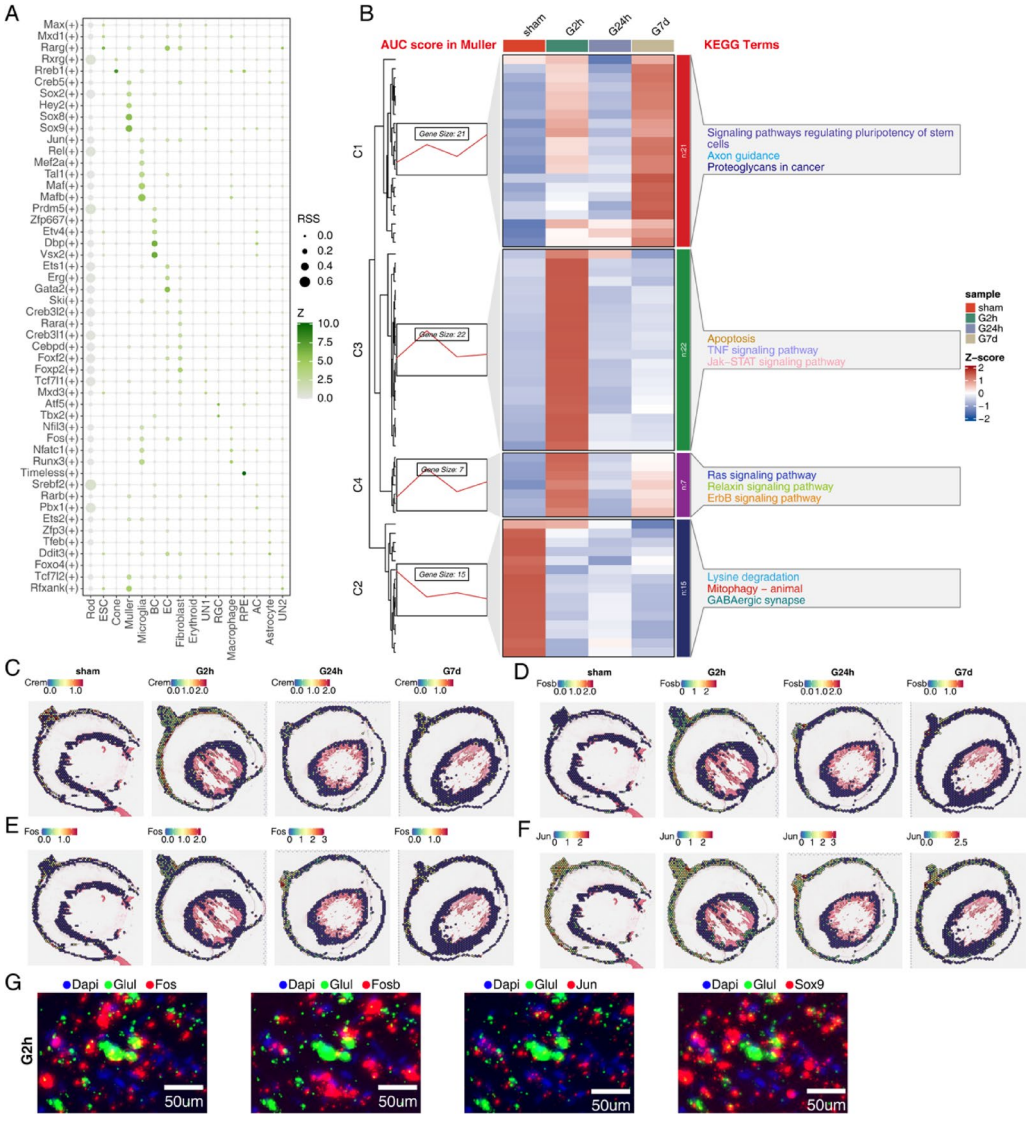

Fig. 4 Expression and regulatory atlas of transcription factors and transcriptional regulons in scRNA-seq. **A** The bubble plot displays the Regulon Specificity Scores (RSS) for key transcription factor regulons across different cell types. The size of the dots represents the RSS value, and the color intensity reflects the Z-score of regulon activity. **B** A clustering heatmap of the expression of transcription factors and target genes, along with the functional pathways enriched by the target genes. **C–F** The expression of the four transcription factors, Crem, Fosb, Fos, and Jun, in ST-seq. (The Z-score reflects the degree of deviation of the transcription factor expression level relative to the overall sample mean and standard deviation. Specifically, a Z-score higher than 0 indicates that the transcription factor's expression level is above average under specific conditions, while a Z-score lower than 0 indicates that the expression level is below average. The larger the absolute value of the Z-score, the greater the deviation from the average, indicating a more significant change in the expression of the transcription factor). **G** MIP-seq validation of the expression of transcription factors Fos, Fosb, Jun, and Sox9 in Müller cells. (glul marks Müller cells) Similar results were observed in at least three independent experiments. The scale bars in the figures are 50 μm

category, while subgroups 0, 2, 5, 6, and 7 form the other category (Fig. 5E). This classification is highly consistent with the distribution of subgroups in the UMAP plot except subgroup 4. Furthermore, differential expression gene analysis revealed that these genes are mainly concentrated in the C0, C1, and C3 subgroups (Fig. 5F).

Cellular communication analysis demonstrated the increased cell–cell communication during the early stages of injury

Intercellular interactions play a direct role in regulating cell states and functions. Therefore, we used CellChat to further investigate the characteristics of intercellular interactions, focusing on seven cell types with established roles in retinal neurodegeneration and sufficient cellular abundance for robust statistical inference: RGCs, ACs, Müller cells, microglia, macrophages,

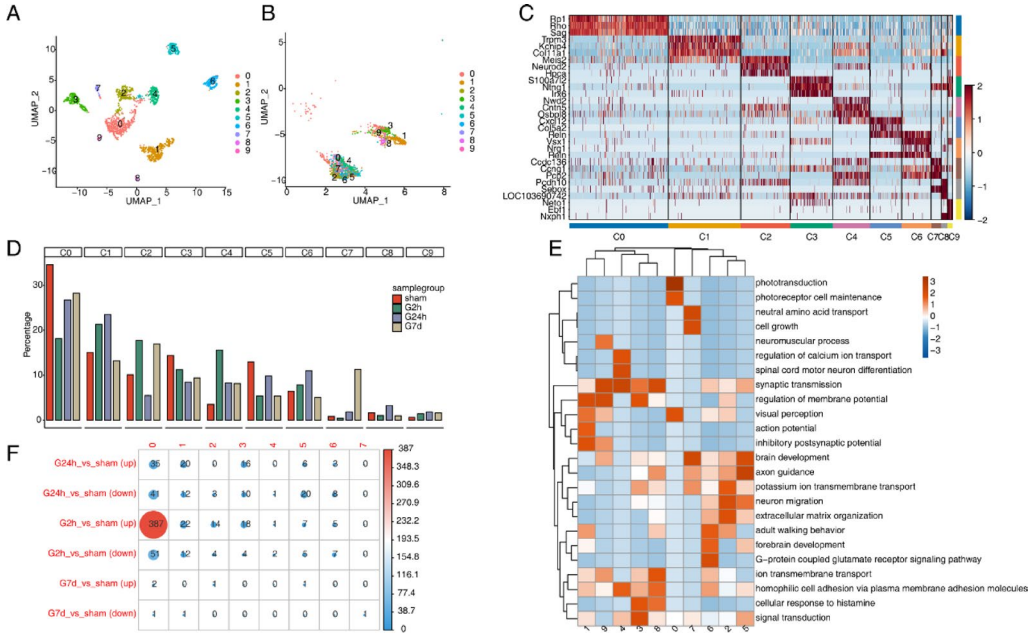

Fig. 5 Subpopulation analysis results of bipolar cells. **A** The UMAP plot shows the subcluster classification and distribution results of BC cells. **B** The UMAP clustering plot shows the projection of the obtained BC cell subpopulations into two major categories. **C** The heatmap displays the expression patterns of the highest-expressed genes in each cell subpopulation. **D** The bar chart shows the proportion distribution and variation characteristics of each BC subpopulation. **E** The heatmap shows the GO functional pathways and characteristics enriched by the highly expressed genes in each BC subpopulation ($log_2FC \geq 0.5$). **F** The bubble plot shows the number of DEGs identified in each BC subpopulation at different time points ($P \leq 0.05$, $log_2FC \geq 0.5$)

BCs, and astrocytes. Cell types with very low abundance (e.g.,erythroid cells, fibroblasts) or primarily phototransductive functions (rod cells, cone cells) were excluded from this focused analysis, as their contributions to acute RGC degeneration were anticipated to be minimal based on our differential expression and spatial co-localization findings. First, we found that I/R injury significantly enhanced the number and strength of cellular interactions compared to the Sham group (Fig. 6A), indicating that I/R injury disrupts the intercellular communication network and cell functions. Combining with the co-localization of RGCs with ACs, Müller cells, macrophages by ST-seq analysis (Fig. 2G), we focused on the interactions among these cell types. The results showed that the interaction strength was obviously enhanced in the G2h and G24h samples, but decreased at G7d, while the interaction between Müller cells and other cells sustains a high level in G7d samples (Fig. 6B). In G7d, the overall intercellular interactions decrease as the proportion of RGCs declines. We hypothesize that the enhanced intercellular interactions triggered by I/R injury may mediate dysfunction in RGCs and other neural cells, leading to their damage and death. Additionally, we analyzed the pairwise interaction relationships between RGCs and other cell populations. The results revealed that interactions from other cells to RGCs, such as App–Sorl1, Ncam1–Ncam1, and Pcdhga5–Pcdhga5, were significantly enhanced at the G2h and G24h stages (Fig. 6C, Figure S9A). Similarly, interactions originating from RGCs also exhibited a comparable trend of changes (Figs. 6D, S9B). Ncam1 (also known as CD56) plays a critical role in mediating programmed cell death processes, including apoptosis [23]. Finally, we focused on analyzing the expression characteristics of the identified ligand-receptor pairs at the cellular level (Fig. S9C-D) and their distribution within the retinal spatial structure. The results showed that Ncam1 is mainly expressed in the optic nerve head region in the Sham and G2h groups, but at G24h and G7d, it shifts to retinal tissue (Fig. 6E). The spatial expression of Ncam2 also showed distinct pattern in several spots of G2h and G7d samples, but shows very low expression in other spots and stages (Fig. S9E). App is mainly expressed at higher levels in the optic nerve head, as well as in the anterior and inner retinal regions (Fig. 6F). L1cam is primarily expressed in the inner retinal layers (Fig. 6G). MIP-seq results further confirmed that Müller cells can interact with RGCs through signaling pathways such as App–Sorl1, Cadm1–Cadm1, and Ncam1–Ncam1 (Fig. 6H). Based on the above results, we propose that early I/R injury significantly disrupts the intercellular interaction network in retinal tissue, activating multiple interaction pathways associated with apoptosis. This disruption can induce cell death in the optic nerve head and retinal tissue, with RGC apoptosis being most prominent. Ultimately, this may trigger the onset and progression of glaucoma.

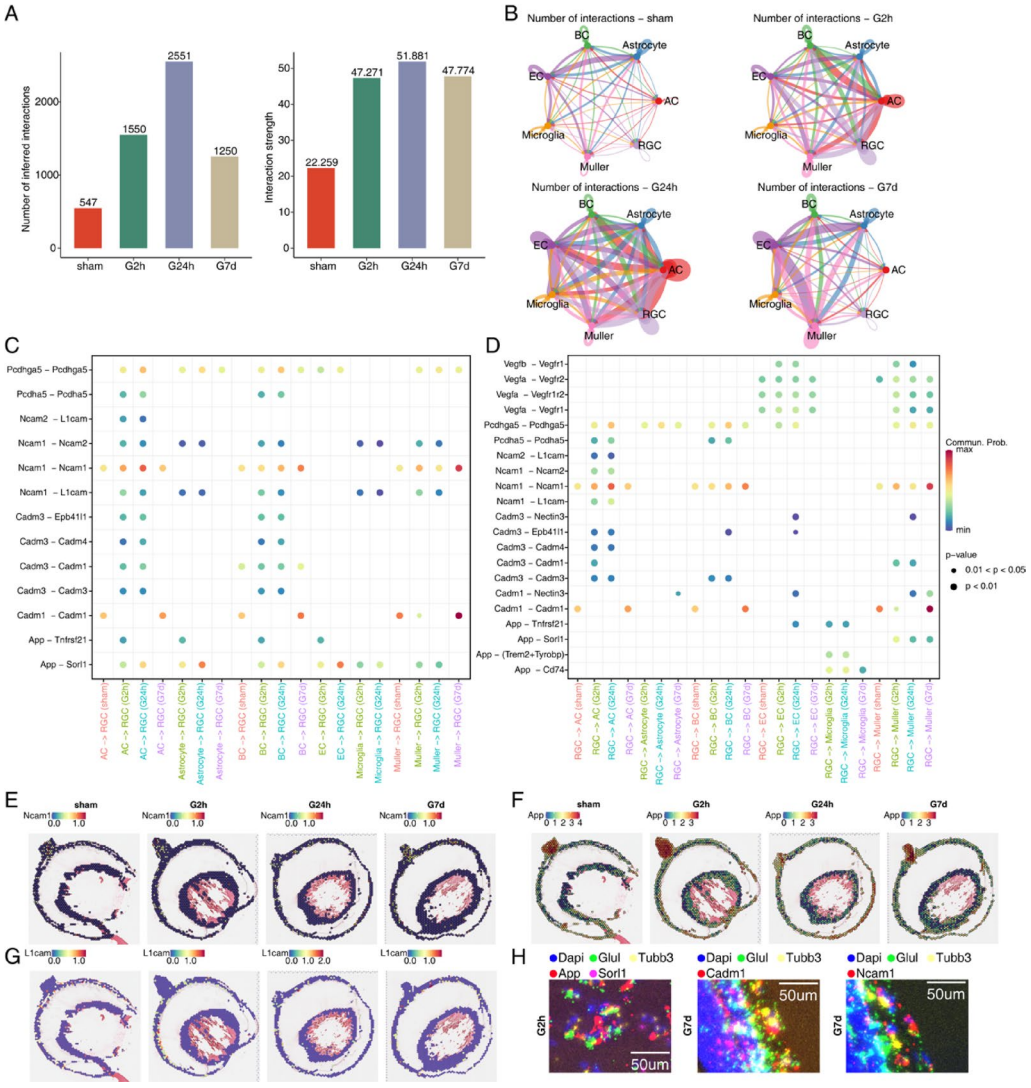

Fig. 6 Intercellular Interaction Map in Retinal Ischemia–Reperfusion Injury in Rats. **A** The bar chart shows how the number and intensity of cell interactions change throughout the I/R injury process. **B** The network plot shows the changes in cell–cell interactions between different types of neurons and glial cells during the I/R injury process. **C–D** The bubble plot shows the characteristic changes in ligand-receptor interactions between RGC and other cell types. **E–G** The expression characteristics of Ncam1, App, and L1cam in ST-seq are shown. **H** MIP-seq validated the interaction between Müller cells and RGC cells. (tubb3 marks RGC; glul marks Müller) Similar results were observed in at least three independent experiments. The scale bars in the figures are 50 μm

Pseudotime analysis revealed the dynamic changing process of AC and RGC cells during ischemia–reperfusion injury

Based on the results that RGCs and ACs show obvious spatial co-localization (Fig. 2G) and frequent intercellular interactions between RGCs and ACs (Fig. 6B, C), we conducted pseudotime analysis to investigate their common and cell-type-specific transcriptional changes throughout the I/R injury dynamic process. Pseudotime analysis orders cells along a trajectory based on transcriptional similarity, modeling the continuum of molecular states as cells respond to injury over time, without implying developmental lineage relationships. Using Monocle2, we classified AC and RGC cells into three distinct states, representing three transcriptional branches along the injury response continuum (Fig. 7A). State 1, which contains the highest proportion of Sham (uninjured) cells (Fig. 7B) and represents the baseline transcriptional state, was set as the root for trajectory ordering. The pseudotime trajectory showed that at the starting stage (State 1), both ACs and RGCs co-localize transcriptionally. However, as the trajectory advances (States 2 and 3), these two cell types gradually diverge toward different branches, reflecting cell-type-specific transcriptional reprogramming in response to I/R injury. Meanwhile, across the four time points, cells in the Sham and G7d samples were predominantly located at the starting phase of the trajectory, while cells in the G2h and G24h samples were

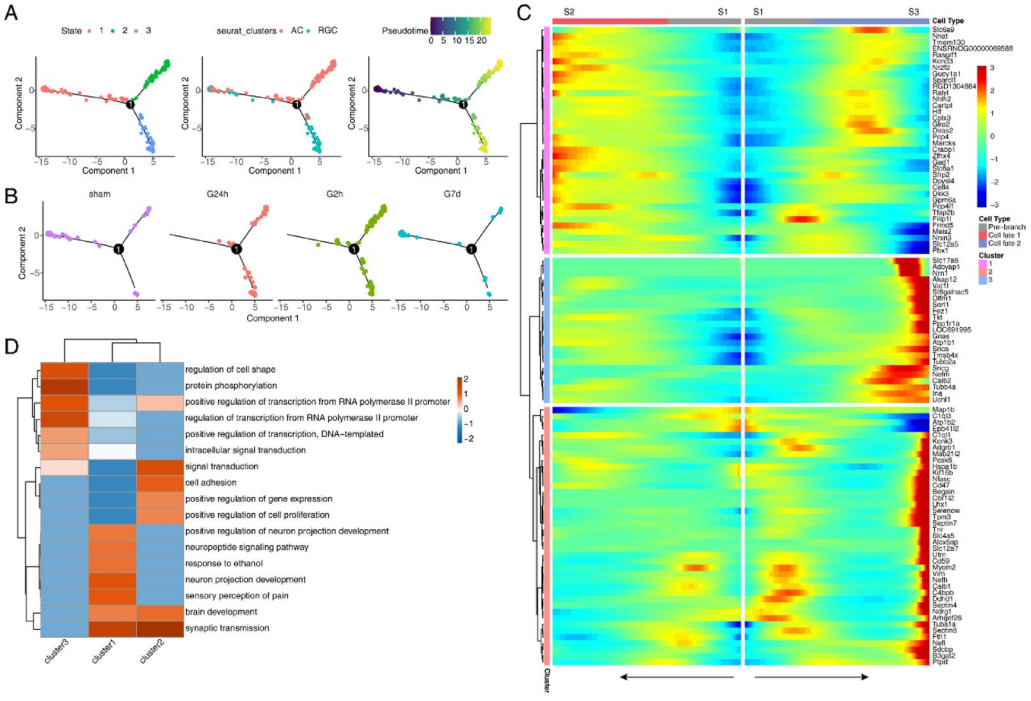

Fig. 7 Pseudo-time analysis map of RGC and AC cell types. **A** The three branches obtained from pseudo-time analysis and the distribution of two cell types across these branches. **B** Distribution of the four time points across the three branches obtained from pseudo-time analysis. **C** The heatmap displays the expression patterns of genes across the three branches with respect to pseudo-time. **D** The heatmap shows the GO functional clustering of genes across the three branches

enriched at the trajectory's endpoint (Fig. 7B). Moreover, we identified clustering patterns of gene expression, key functional genes (Fig. 7C), and their enriched biological pathways during the progression of the trajectory (Figs. 7D, S10). The results revealed that one group of genes leading to branch S2 was highly expressed at the end of the trajectory, while two other gene groups leading to branch S3 also exhibited high expression levels at the end (Fig. 7C). These results suggest that the impact of I/R injury on ACs and RGCs is primarily concentrated at the G2h and G24h stages, with this effect weakening at G7d.

Discussion

This study presents the first integrated spatiotemporal atlas of retinal ischemia–reperfusion (I/R) injury, combining single-cell and spatial transcriptomics to delineate dynamic cellular, molecular, and spatial interactions driving neuronal degeneration. Our findings reveal critical insights into the cellular and gene expression changes that occur throughout the injury progression, highlighting novel cellular interactions and gene networks that could provide potential therapeutic targets for glaucoma and related retinal diseases.

Our results demonstrate that retinal I/R injury induces substantial changes in the composition of retinal cell populations. Among the 14 identified cell types, we observed a dynamic shift in their abundance across different stages of I/R injury. Notably, retinal ganglion cells (RGCs), Müller cells, and microglia exhibited significant temporal changes, consistent with previous findings linking these cells to retinal degeneration and inflammatory responses [24, 25]. RGCs, which are critical to visual function and are the primary cell type affected by I/R injury, displayed distinct expression profiles related to apoptosis, oxidative stress, and autophagy pathways, particularly at the 2 h and 24 h' time points post injury.

The spatial transcriptomic analysis further provided an invaluable perspective on how these cellular changes manifest in the retinal architecture. The cell2location deconvolution method allowed us to map the spatial distribution of key cell types, revealing that RGCs predominantly localize to the inner retina and optic nerve head region, while Müller cells share a similar distribution [15]. Interestingly, the early stages of injury (G2h and G24h) were marked by enhanced cellular interactions, with RGCs co-localizing with microglia, macrophages, and Müller cells. These interactions were particularly prominent in regions associated with apoptosis and neurodegeneration, suggesting their potential role in mediating RGC death. By integrating scRNA-seq and ST data, we provided compelling evidence that the disruption of cell–cell communication, especially between RGCs and amacrine cells, Müller cells, and microglia, may play a critical role in retinal pathology during I/R injury.

The integration of single-cell and spatial transcriptomics in this study provides a novel perspective on retinal I/R injury compared to traditional methods. Previous studies have focused on the temporal expression patterns of individual genes or single time points of single-cell omics, often without considering the spatiotemporal context of these changes [2, 6, 7]. Our study builds upon this foundation by providing a detailed map of cellular dynamics and their corresponding gene expression changes at multiple time points, which is essential for understanding the disease progression in glaucoma and similar retinal pathologies. In particular, our findings highlight the role of specific transcription factors, such as Sox9 and Sox8 in Müller cells, and their involvement in regulating apoptosis, TNF signaling, and autophagy during the early stages of I/R injury, aligning with previous studies that have implicated these pathways in retinal degeneration [26–28].

One of the most significant findings in this study is the dynamic expression of key genes associated with oxidative stress, such as Gpx1, Arl6ip5, and Mapt, in RGCs. These genes showed specific spatiotemporal patterns of expression, which were previously underexplored in the context of retinal I/R injury. While other studies have examined oxidative stress in retinal injury models [29, 30], our study is the first to integrate this data with cellular localization, offering a more comprehensive understanding of how these processes unfold in the retinal microenvironment.

The identification of key molecular drivers of RGC death during I/R injury offers important insights into the pathogenesis of glaucoma and other retinal diseases. In particular, the upregulation of apoptosis-related genes and the specific involvement of autophagy and oxidative stress pathways suggest that therapeutic strategies targeting these pathways could be effective in mitigating retinal damage. In addition, the observed disruption in cell–cell communication, particularly in the interactions between RGCs and Müller cells, provides a novel avenue for future therapeutic interventions [31, 32]. Targeting these aberrant interactions may prevent the progressive loss of retinal cells and improve long-term visual outcomes.

Moreover, the identification of critical transcription factors such as Sox9 and Sox8, which are activated early during I/R injury, underscores the potential of targeting these factors to modulate retinal cell function and survival. These findings may inspire the development of gene-based therapies aimed at modulating retinal cell responses during injury, offering new opportunities for clinical intervention [33].

Limitations and future directions

Despite the comprehensive nature of this study, there are several limitations that must be acknowledged. First, the relatively small sample size limits the statistical power of some of our analyses. Future studies should increase the sample size to confirm the robustness of our findings across a broader population. Second, while our multi-omics approach provides a powerful, high-resolution map of spatiotemporal dynamics and generates strong mechanistic hypotheses, it does not constitute functional or protein-level validations. Future studies employing techniques such as cell-type-specific knockout/knockdown of key genes (e.g., Ncam1, Sox9) identified here, or the use of neutralizing antibodies against specific ligand-receptor pairs, will be essential to definitively establish causal relationships and therapeutic potential.

Additionally, the 10 × Genomics Visium platform used lacks single-cell resolution and depends on algorithms to integrate spatial transcriptomics and scRNA-seq data to estimate the enrichment probability of cell types within spatial spots, providing probabilistic estimates instead of precise localization. Therefore, future research should focus on computational algorithms and the development of higher-resolution and high-throughput spatial technologies to overcome challenges such as platform differences and data standardization.

Finally, while our findings offer important insights into retinal I/R injury, the clinical application of these results remains an ongoing challenge. Future research should aim to translate these findings into effective treatments, potentially through the development of targeted pharmacological interventions or gene therapies that can modulate the identified pathways.

Conclusion

In conclusion, this study presents a detailed, spatiotemporally resolved map of retinal cellular dynamics and gene expression changes during I/R injury, providing new insights into the molecular mechanisms underlying retinal degeneration and glaucoma. By integrating single-cell and spatial transcriptomics, we have identified potential therapeutic targets, including key transcription factors, oxidative stress-related genes, and disrupted cell–cell interactions, that could inform the development of more effective treatments for retinal diseases. Future research will be needed to validate these findings and explore their therapeutic potential in clinical settings.

Methods

Animals

Seven-week-old male Sprague–Dawley rats were purchased from the Guangdong Animal Experiment Center, all of which were healthy and free of eye diseases. They were fed standard chow and provided free access to water, ensuring they had adequate food and hydration. The temperature was maintained at 24 ± 1 °C, with humidity ranging from 45 to 50%. The light–dark cycle

in the breeding environment was set to 12 h (lights on at 07:00, lights off at 19:00). All animals were housed in a specific pathogen-free facility at the Jinan University Animal Laboratory. All experimental procedures strictly followed the National Laboratory Animal Protection Regulations, the statement of the Association for Research in Vision and Ophthalmology (ARVO), the relevant guidelines of the Jinan University Laboratory Animal Committee (approval number: JN-A-2002-01) and Xiangya School of Medicine, Central South University (Ethical Approval Code: xy2023101236).

Construction of retinal ischemia–reperfusion injury model

The retinal ischemia–reperfusion injury model was established as described earlier. In brief, anesthetized rats with dilated pupils and corneal anesthesia were placed on a heated workstation. A 31G needle connected to a saline infusion device was carefully inserted into the rat's anterior chamber. By adjusting the height of the saline bottle (151 cm), the intraocular pressure was gradually increased to 110 mmHg and maintained for 60 min. The pressure was maintained for 60 min. The sham-operated control group underwent the same procedure, but without saline pressure infusion. During and after the surgery, 0.3% tobramycin eye ointment (Alcon, USA) was applied to keep the eyes moist and prevent infection [34]. The success of the I/R model and the resulting retinal degeneration were confirmed by a significant reduction in both the b-wave amplitude of electroretinography (ERG) and the thickness of the ganglion cell complex (GCC) at later time points, as shown in Supplementary Figure.

Histological examination

After anesthetizing the rats, they were subjected to cardiac perfusion with pre-cooled physiological saline. The intact eyeballs were collected and fixed overnight at 4 °C in FAS eyeball fixation solution (G1109, Servicebio, Wuhan, China). The fixed eyeballs were subsequently dehydrated, embedded in paraffin, and sectioned at 10 μm thickness in the retinal-optic nerve plane for each sample.

Hematoxylin and eosin (H&E) staining was performed on the retinal sections using a Hematoxylin–Eosin staining kit (G1005, Servicebio, Wuhan, China). To better characterize the morphological changes in the retina, the thickness of the retinal sections and the ganglion cell complex (GCC), consisting of the retinal nerve fiber layer, ganglion cell layer, and inner plexiform layer (which exactly corresponds to the anatomical distribution of RGCs in the retina) was measured using Image-Pro Plus 6.0 software (Media Cybernetics, Rockville, MD, USA) (Figure S1D). The parameters included: perpendicular to the retinal pigment epithelium and at distances of ± 700, ± 1400, ± 2100, ± 2800, ± 3500, and ± 4200 μm from the optic nerve center. For each analysis, three measurements were taken from each image, and the average was then calculated [35, 36].

Electroretinography (ERG) detection

Retinal function was monitored using a full-field flash electroretinogram (ERG) (GT-2008 V-VI, Gotec, Chongqing, China). Dark adaptation was performed under dim red light, as previously described. The anesthetized rat was placed on a flat platform, with the reference electrode positioned subcutaneously at the occipital region and the ground electrode placed at the base of the tail. The contact lens, including a silver wire recording electrode, was attached to the center of the cornea. Visual flash ERG was recorded at light intensities of 0.1, 1, 3, and 10 cd.s/m^2. For light intensities between 0.1 and 3 cd, four measurements were made for each intensity. One measurement was taken at 10 cd. After the preceding light stimulus, the light intensity was increased for 60 s. The amplitudes of the a-wave and b-wave were recorded at the end [35].

Retinal single-cell sample collection and suspension preparation

For the retinal single-cell suspension, eyes were collected from deeply anesthetized rats at 2 h, 24 h, or 168 h (7 days) following retinal I/R injury. For each time point, retinas from three individual rats (one eye per rat) were processed independently into single-cell suspensions, which were then pooled together prior to library construction to create one sequencing library per time point. Eyes were also collected from sham-operated rats that did not undergo physiological saline pressure infusion, serving as controls. The cornea, iris, lens, and vitreous were excised, and the retina was carefully separated from the posterior eye globe. A 2-mm biopsy punch (Robbins Instruments, Houston, TX, USA) was used to carefully excise the central portion of the retina to prepare the single-cell suspension.

In brief, the retina was incubated with activated papain at 37 °C for 45 min, followed by gentle trituration (using a 10 mL pipette to move up and down approximately 10–20 times). After centrifuging the cells at 300 × g for 5 min, papain was removed by adsorption, and the cells were then resuspended in medium containing 10% ovomucoid, a papain inhibitor containing 5% DNase I. Complete cells were separated from the cell membrane through single-step discontinuous density gradient centrifugation at 100 × g for 6 min. To reduce acute, endogenous transcriptional changes, we applied the general transcription inhibitor actinomycin D during the dissociation process. Actinomycin D inhibits transcription mediated by all three eukaryotic RNA polymerases, offering broad-spectrum, rapid transcriptional inhibition with

minimal and slow reversibility. Actinomycin D (Sigma-Aldrich, St. Louis, MO, USA; Cat# A1410) was added at three steps during the dissociation process: 45 mM to the papain solution, 45 mM to the papain inhibitor solution, and 3 mM during trituration.

After centrifugation, the supernatant was removed, and the cell pellet was resuspended in 100 µL of dead cell removal microbeads (Miltenyi Biotec, USA; No. 130–090-101). The cell suspension was then passed through an MS column (Miltenyi Biotec, USA, No. 130–042-201), placed in the magnetic field of the appropriate MACS separator (Miltenyi Biotec, USA, No. 130–042-109). The MS column was eluted with 1 × binding buffer. The cells were collected as the live cell fraction. The live cells were separated by centrifugation at 70 × g for 6 min at room temperature, and the resulting pellet was resuspended in Dulbecco's phosphate-buffered saline containing 0.4% BSA. Finally, cell viability was assessed using AO/PI staining on a cell counter (Nexcelom Bioscience LLC, Lawrence, MA, USA). The final concentration reached 100,000 cells/mL, with a viability rate exceeding 80% [37].

Single-cell library construction and sequencing

The single-cell library was prepared according to the BD Rhapsody Single-Cell 3' Full Transcriptome WTA Library Construction Standardized Manual. After passing quality control, the library was sequenced using the PE150 mode on the Illumina Nova Seq6000 sequencing platform.

raw data processing

The BD Rhapsody pipeline (https://bitbucket.org/CRSwDev/cwl/src/master/v2.0/) was used to generate a digital gene expression matrix. The UMI count matrix was converted into a Seurat object by the R package Seurat (version 4.3.0). Cells with UMI numbers < 1000 or with detected genes < 500 or with over 15% mitochondrial-derived UMI counts were considered low-quality cells and were removed. Genes detected in less than 5 cells were removed for downstream analyses.

After quality control, the UMI count matrix was normalized using SCTransform. Then we conducted data integration through the harmony algorithm based on gene expression profiling. To reduce the dimensionality of the scRNA-Seq dataset, principal component analysis (PCA) was performed on an integrated data matrix. With Elbowplot function of Seurat, top 50 PCs were used to perform the downstream analysis. The main cell clusters were identified with the FindClusters function offered by Seurat, with resolution set as default (res = 0.4), and they were visualized by UMAP plots. To identify the cell type for each cluster, we detected gene markers for each cell clusters using the "FindMarkers" function in Seurat package, then we annotated cell types using ScType tools [38–41]. Cell type annotation was performed using a set of canonical marker genes, identified from the integrated dataset across all conditions, to define stable core cellular identities (Table S1).

Differential gene expression analysis

Differentially expressed genes (DEGs) were determined with the FindMarkers/FindAllMarkers function from the Seurat package (one-tailed Wilcoxon rank sum test, *p*-values adjusted for multiple testing using the Bonferroni correction). For computing DEGs, all genes were probed that the expression difference on a natural log scale was at least 0.5 and adjusted *p*-value was less than 0.05.

Transcription factor regulatory network analysis

The modules of TFs were identified by the SCENIC python workflow (version 0.11.2) using default parameters (http://scenic.aertslab.org). A rat TF gene list was used from the resources of pySCENIC (https://github.com/aertslab/pySCENIC/tree/master/resources). Activated TFs were identified in the AUC matrix, and differentially activated TFs were selected using "FindAllMarkers" of the Seurat package [21]. Briefly, SCENIC first identifies co-expression modules between transcription factors and potential target genes using GENIE3. Subsequently, cis-regulatory motif analysis (cisTarget) is applied to retain only those target genes that contain binding motifs for the corresponding transcription factor in their promoter regions, thereby inferring direct transcriptional targets. The activity of each regulon (TF plus its target genes) in individual cells was quantified using AUC (Area Under the Curve) scores.

Cell–cell communication

Cell–cell communication analysis was performed using CellChat (v2.1.2) [42] with default parameters and the precompiled mouse ligand-receptor interaction database provided within the package. Briefly, the communication probability was calculated using the computeCommunProb function with default settings, and the cell–cell communication network was subsequently inferred and aggregated using default parameters. Key parameters included a minimum edge probability of 0.5, a maximum path length of 2 for indirect signaling, a p-value threshold of 0.05, 100 bootstrap iterations, interaction range constraints, distance normalization, and a minimum of 10 interacting pairs (k.min = 10). The number of interactions was visualized to represent the aggregated cell–cell communication network and signaling patterns from each cell cluster. Given the quality of the scRNA-seq data and the biological relevance to I/R-induced neurodegeneration, seven cell types with sufficient cell numbers (> 100 cells per condition) and established roles in retinal pathology were included in the analysis: retinal ganglion

cells (RGCs), amacrine cells (ACs), Müller cells, microglia, macrophages, bipolar cells (BCs), and astrocytes. This focused selection ensured statistical robustness while maintaining biological relevance to the research question.

Pseudotime analysis

Monocle2 was used for pseudotime analysis, trajectory construction, and calculation of pseudotime-dependent gene expression (Monocle2, version 2.26.0). DDRTree (version 0.1.5) method is used for dimension reduction. Cell trajectory was visualized according to cell subtypes and cell states. The Basic Differential Analysis algorithm is used to identify differently expressed gene according to pseudotime function. BEAM (Branched Expression Analysis Modeling) was used to identify genes that are regulated in a branching-dependent manner [43].

Collection of eye samples for spatial transcriptomics and slide preparation

Eyes were collected from deeply anesthetized rats 2 h, 24 h, or 168 h (7 days) after retinal ischemia–reperfusion injury. For spatial transcriptomics, one eye from one rat was used per time point (Sham, G2h, G24h, G7d), constituting independent biological replicates for the ST analysis. Eyes were also collected from sham-operated rats that did not undergo physiological saline pressure infusion, serving as controls. The eyes were then embedded in Tissue TEK OCT compound (VWR Cat No. 25608–930) and rapidly frozen on dry ice. The eyes were stored at -80 °C for future analysis. The dorsal and temporal sides of the entire eye were marked with tissue labeling dye for experiments requiring anatomical orientation information.

The spatial transcriptomics library was prepared using the 10 × Genomics Visium Spatial Gene Expression Kit. After tissue embedding, cryosectioning, and fixation of the rat eyeballs, optimized tissue slides were obtained. These slides were calibrated using the Aperio VERSA 200 scanning system, followed by bright-field imaging at 5 × magnification with a 200 ms exposure time. The entire tissue capture area was imaged in one shot, producing clear images of the tissue. Subsequently, the permeabilization experiment was completed with the same settings, and clear fluorescence images were obtained. It was observed that at 12 min, the fluorescence signal was strongest and signal diffusion was lowest, making this time point the optimal tissue permeabilization time.

10 × Genomics visium library preparation and sequencing

For preparing the Visium slides, the tissue block was equilibrated to -18 °C, and 10 μm thick sections were placed on the active sequencing area (6.5 mm × 6.5 mm) of the 10 × Genomics Visium slide. The slides were stored at -80 °C in an airtight container until the time for spatial library generation. Hematoxylin and eosin (H&E) staining was performed following the 10 × Genomics Visium protocol. The RIN values for all Visium-treated samples were greater than 8.7. In brief, the sections were fixed with cold methanol, stained with H&E, and imaged on the Hamamatsu NanoZoomer S60. Following this, a template-switching protocol was used for permeabilization, reverse transcription, and cDNA synthesis. The second-strand cDNA was released from the slide, and a single-index library was prepared using the 10 × Genomics PCR-based protocol. Sequencing of the library was conducted on the HiSeq 4000 (1 read per lane), with a target of 300 M raw reads per sample. The sequencing format was as follows: read 1: 28 cycles; i7 index read: 10 cycles; i5 index read: 10 cycles; and read 2S: 50 cycles. The cleaned data were subsequently processed using 10 × Genomics Space Ranger (version 2.3.1) software for cell quality control, identification, and alignment with the rat reference genome (rat_NCBI_v7.2), generating the raw expression matrix. The matrix was then subjected to in-depth downstream analysis using the Seurat package (version 4.3.0) [44].

Single-slide processing

Filtered feature-barcode expression matrices from SpaceRanger (v2.3.1) were used as initial input for the spatial transcriptomics analysis using Seurat (v4.3.0). The data filtering criteria were as follows: (1) Genes with less than 10 spot expressions were filtered out; (2) Spots with less than 300 measured genes and less than 500 UMIs were filtered out. Ribosomal and mitochondrial genes were excluded from this analysis. Individual count matrices were normalized, screened for hypervariable genes, and normalized using sctransform. PCA was used to reduce the dimension of the data, and the first 30 PCS were selected for clustering. Then, the spots of the 4 samples were integrated by the CCA algorithm IntegrateData function to display the clustering results of the batches with single sample tissue slices and UMAP dimension reduction, and the resolution was uniformly set to 0.5.

Spatial gene expression data processing and analysis using Cell2location

To spatially resolve cell populations identified in the scRNA-seq, we used Cell2location (v0.1.3) [15] to estimate cell type abundance for each spatial slide by taking a spatial expression matrix with mRNA counts of genes at spatial locations and a matrix of reference cell type signatures as input. All Cell2location analyses were conducted using Scanpy (v1.9.3). Before running Cell2location to map our reference cell types to each ST-seq dataset, both the estimated reference cell type signatures (gene expression) and ST-seq dataset from each respective biopsy were filtered to select genes shared between the two data

objects. The filtered objects were both used as input to Cell2location.

To estimating reference cell type signatures, the scRNA-seq reference signatures of cell types were loaded into Scanpy using sc.read_h5ad. First, the regression model for the single cell data was initialized with default settings, using batch as the batch_key and the model was trained using a maximum of 250 epochs. Next, the regression model for the ST-seq data was initialized with the scRNA-seq reference signatures by default settings and hyperparameters selected based on cell2location's recommendations. Model accuracy was evaluated based on the evidence lower bound (ELBO) loss and reconstruction accuracy plots. We did not observe strong within-batch variation in total RNA counts, therefore we set detection_alpha = 200 and batch_size = 2500. By manual visual inspection, we estimated the number of cells per spot to be 16 and set N_cells_per_location = 16. The model was then trained using a maximum of 30,000 epochs. Cell2location's Non-negative Matrix Factorization (NMF) was used to identify cellular compartments and cell types that co-locate from the cell type abundance estimates, using n_fact = 12.

MiP-seq tissue preparation

Samples, served as subjects for ISS sample preparation from eyes. Animals were euthanized via isoflurane administration, followed by perfusion using a solution of 4% paraformaldehyde (PFA) in phosphate-buffered saline (PBS). The eyes were carefully extracted and subsequently post-fixed in 4% PFA for a duration of 12 h at 4 ℃. Cryoprotection was achieved using a 30% sucrose solution in PBS. Once embedded in an optimal cutting temperature (OCT) compound, the tissues were sectioned coronally to a thickness of 10 μm using a Leica cryostat. Sections encompassing retina were preserved at − 80℃, pending ISS.

Prior to ISS analysis, eye slices underwent the following preparatory procedure: Initially, slices were sealed within Secure-Seal hybridization chambers. Subsequent to this, they were rinsed twice with ice-chilled DEPC-PBS, followed by a fixation period of 10 min in 4% PFA. Post-fixation, the slices were subjected to three washes using DEPC-OBSTR (PBS supplemented with 0.1%Tween-20 and 0.1 U/μl RRI). Thereafter, the slices were immersed in pre-cooled methanol and maintained at -80℃ for a span of 15 min. Subsequently, the slices were exposed to a solution of 2 mg/ml pepsin (Sigma, P0525000) in 0.1 M HCl and incubated at 37℃ for 90 s. After a final rinse with DEPC-PBSTR, the tissue slices were aptly conditioned for ISS analysis [45].

MiP-seq probe design

For ISS analysis, a set of specific genes from retina were chosen. The probe assembly employed in ISS is comprised of a duo of padlock probes paired with an RCA initiator primer probe, specifically designed for target-dependent RCA. Additionally, detection probes for RCA and in situ sequencing probes were incorporated. The design methodology for these probes has been reported in prior publications. Briefly, the ISS probes were generated according to the following criteria: (1)Exons located near the 5'end were preferred, with two target sites selected for each gene. (2) The padlock probe had complementary ends (12–16 bp) that matched the target sequence, while the middle section consisted of a complementary anchor primer sequence and a barcode sequence, (3) The RCA initiator primer had a 5' end that matched the 3' end of the target sequence (12–16 bp), and its 3' end complemented the padlock probe. (4) The efficiency of RCA was assessed using the detection probe (cy3-p4). (5) The probes for in situ sequencing included three anchor primers (anchor-1, anchor-2, and anchor-3) and four query probes (seg-1, seg-2, seg-3.and seg-4), each labeled with different Alexa Fluor dyes.

In situ sequencing

The ISS procedures we used were described previously. Briefly, padlock probes were first phosphorylated at their 5' termini using T4 polynucleotide kinase (Vazyme, N102-472 01). Subsequently, the phosphorylated padlock probes, at a concentration of 30 nM per probe, were combined with the RCA initiator (also 30 nM per probe) in a hybridization buffer comprising 2 × SSC (SangonB548109), 10% formamide (Sangon, A100606), and 20 mM RVC (Bevotime, R0108). This mixture was added to a hybridization chamber housing pretreated eye slices and incubated overnight at 37 °C. Following this, the samples underwent two wash cycles with DEPC- PBSRT, succeeded by a 4X SSC wash. The chamber then received ligase reaction mixture for a 2 h incubation at 37 °C. After an additional two wash cycles with DEPC-PBSTR, the samples were treated with a rolling circle amplification reaction solution, comprised of 1 U/μl Phi29 (Vazyme, N106-01), 1X RCA buffer, 0.25 μM dNTP, 0.2 μg/μl BSA, and 5% glycerol, for 2 h at 30℃. Post-wash, the samples were exposed to a sequencing mixture, containing 1X BSA, 0.2 U/μl T4 DNA ligase (Thermo Fisher Scientific, EL0012), 1X T4 DNA ligase buffer, 1 μM anchor primer, and 1 μM query primer for a 2 h incubation at 25℃. The samples were then thrice washed using a 10% formamide in 2X SSC solution, followed by DAPI staining. Imaging was conducted on a Leica THUNDER Imaging Systems, 20 × (NA = 0.80). After each imaging round, signals were eradicated with a stripping buffer (60% formamide in 2X SSC) twice for

10 min at ambient temperature. This was followed by the addition of the subsequent round's sequencing mixture to facilitate multiple sequencing rounds.

Retrograde labeling RGCs by superior colliculus injection

Three days prior to sacrifice, rats were anesthetized and secured in a stereotaxic apparatus (RWD Life Science, Shenzhen, China) using blunt ear bars. A volume of 0.5 μL of 4% Fluoro-Gold (FG; Fluorochrome, Denver, CO, USA) solution was then slowly injected into the superior colliculi bilaterally at the following coordinates relative to bregma: 6.0 mm posterior, 1.8 mm lateral to the midline, and 4.0 mm deep from the skull surface, as previously described [36]. Three days post-injection, the retinas containing retrogradely labeled FG(+) cells were collected and flat-mounted on microscope slides. FG-positive retinal ganglion cells (RGCs) were visualized using a fluorescence microscope (DM5000 B; Leica, Wetzlar, Germany). For each retina, twelve images were captured at specified radial distances from the optic disc (0.625 mm, 1.25 mm, and 1.875 mm, representing central to peripheral retina) within the superior, inferior, nasal, and temporal quadrants. FG-labeled RGCs in each micrograph were counted using Image-Pro Plus 6.0 software.

Statistical analysis

We used the Shapiro–Wilk test to assess whether the quantitative data followed a normal distribution. Quantitative data that followed a normal distribution were presented as the mean ± standard error of the mean (SEM). To compare count data between two groups, an independent samples t-test was used for normally distributed data, while a non-parametric test (Wilcoxon rank-sum test) was applied to data that did not follow a normal distribution. Correlation analysis of signaling pathway activity intensity in different directions was performed using Spearman's correlation coefficient test. The correlation between gene expression levels and signaling pathway activity was analyzed using linear regression and Pearson's correlation test. A two-tailed P-value less than 0.05 was considered statistically significant. Statistical analysis was conducted using SPSS 25.0 software (SPSS Inc., Chicago, IL), and data processing was performed using GraphPad Prism 8.0 software (GraphPad Software, San Diego, CA).

Supplementary Information

The online version contains supplementary material available at https://doi.org/10.1186/s13578-026-01571-6.

Supplementary Material 1

Supplementary Material 2

Acknowledgements
We would like to express our sincere gratitude to all the staff members of the Shenzhen Eye Hospital.

Author contributions
Conceptualization: Yijia Huang, Jiantao Wang. Experiments performing: Yijia Huang, Junhong Guo, Fei Yao. Manuscript drafting: Yijia Huang, Junhong Guo, Fei Yao. Data analyzing: Yijia Huang, Junhong Guo, Fei Yao. Project planning: Yijia Huang, Bingkai Feng, Di Gong, Kuanrong Dang, Tingyu Hu, Simin Deng, Yong Liu. Chunyan Tan, Jiantao Wang revised the manuscript. All authors read and approved the final manuscript.

Funding
This work was funded by the Shenzhen Fund for Guangdong Provincial High-level Clinical Key Specialties (SZGSP014), the National Natural Science Foundation of China (82201182), the Shenzhen Key Medical Discipline Construction Fund (SZXK037), the Shenzhen Science and Technology Program (JCYJ20220818103207015), the Shenzhen Science and Technology Program (KCXFZ20230731093359004), the Sanming Project of Medicine in Shenzhen (SZSM202311012), the Natural Science Foundation of Hunan Province, China (2024JJ6670), the Basic Research Project of Shenzhen (JCYJ20240813152617023) and the Sanming Project of Medicine in Shenzhen (SZSM202411009).

Data availability
The datasets used and analyzed during the current study are available from the corresponding author on reasonable request.

Declarations

Consent for publication
Not applicable.

Ethical approval and consent to participate
All animal experiments were approved by the Jinan University Laboratory Animal Committee (approval number: JN-A-2002-01) and Xiangya School of Medicine, Central South University (Ethical Approval Code: xy2023101236).

Competing Interests
The authors declare that they have no competing interests.

Received: 12 August 2025 / Accepted: 29 March 2026
Published online: 09 April 2026

References

1. Osborne NN, et al. Retinal ischemia: mechanisms of damage and potential therapeutic strategies. Prog Retin Eye Res. 2004;23:91–147. https://doi.org/10.1016/j.preteyeres.2003.12.001.
2. Kim BJ, Braun TA, Wordinger RJ, Clark AF. Progressive morphological changes and impaired retinal function associated with temporal regulation of gene expression after retinal ischemia/reperfusion injury in mice. Mol Neurodegener. 2013;8:21. https://doi.org/10.1186/1750-1326-8-21.
3. Wakabayashi T, et al. Intravitreal bevacizumab to treat iris neovascularization and neovascular glaucoma secondary to ischemic retinal diseases in 41 consecutive cases. Ophthalmology. 2008;115:1571–80. https://doi.org/10.1016/j.ophtha.2008.02.026.
4. Palmhof M, et al. Retinal ischemia triggers early microglia activation in the optic nerve followed by neurofilament degeneration. Exp Eye Res. 2020;198:108133. https://doi.org/10.1016/j.exer.2020.108133.
5. Renner M, et al. Optic nerve degeneration after retinal ischemia/reperfusion in a rodent model. Front Cell Neurosci. 2017;11:254. https://doi.org/10.3389/fncel.2017.00254.
6. Andreeva K, et al. Time-dependent gene profiling indicates the presence of different phases for ischemia/reperfusion injury in retina. Ophthalmol Eye Dis. 2014;6:43–54. https://doi.org/10.4137/oed.S17671.
7. Li Y, et al. Single-cell RNA sequencing reveals a landscape and targeted treatment of ferroptosis in retinal ischemia/reperfusion injury. J Neuroinflammation. 2022;19:261. https://doi.org/10.1186/s12974-022-02621-9.

8. Qing KX, et al. Integrated bioinformatics analysis of retinal ischemia/reperfusion injury in rats with potential key genes. BMC Genomics. 2024;25:367. https://doi.org/10.1186/s12864-024-10288-0.
9. Voigt AP, et al. Single-cell RNA sequencing in vision research: insights into human retinal health and disease. Prog Retin Eye Res. 2021;83:100934. https://doi.org/10.1016/j.preteyeres.2020.100934.
10. Baysoy A, Bai Z, Satija R, Fan R. The technological landscape and applications of single-cell multi-omics. Nat Rev Mol Cell Biol. 2023;24:695–713. https://doi.org/10.1038/s41580-023-00615-w.
11. Vandereyken K, Sifrim A, Thienpont B, Voet T. Methods and applications for single-cell and spatial multi-omics. Nat Rev Genet. 2023;24:494–515. https://doi.org/10.1038/s41576-023-00580-2.
12. Gulati GS, D'Silva JP, Liu Y, Wang L, Newman AM. Profiling cell identity and tissue architecture with single-cell and spatial transcriptomics. Nat Rev Mol Cell Biol. 2025;26:11–31. https://doi.org/10.1038/s41580-024-00768-2.
13. Zormpas E, Queen R, Comber A, Cockell SJ. Mapping the transcriptome: realizing the full potential of spatial data analysis. Cell. 2023;186:5677–89. https://doi.org/10.1016/j.cell.2023.11.003.
14. Lukowski SW, et al. A single-cell transcriptome atlas of the adult human retina. EMBO J. 2019;38:e100811. https://doi.org/10.15252/embj.2018100811.
15. Kleshchevnikov V, et al. Cell2location maps fine-grained cell types in spatial transcriptomics. Nat Biotechnol. 2022;40:661–71. https://doi.org/10.1038/s41587-021-01139-4.
16. Yu DY, et al. Retinal capillary perfusion: spatial and temporal heterogeneity. Prog Retin Eye Res. 2019;70:23–54. https://doi.org/10.1016/j.preteyeres.2019.01.001.
17. Reichenbach A, Bringmann A. New functions of Müller cells. Glia. 2013;61:651–78. https://doi.org/10.1002/glia.22477.
18. Weinreb RN, Aung T, Medeiros FA. The pathophysiology and treatment of glaucoma: a review. JAMA. 2014;311:1901–11. https://doi.org/10.1001/jama.2014.3192.
19. Strang KH, Golde TE, Giasson BI. MAPT mutations, tauopathy, and mechanisms of neurodegeneration. Lab Invest. 2019;99:912–28. https://doi.org/10.1038/s41374-019-0197-x.
20. Crack PJ, et al. Increased infarct size and exacerbated apoptosis in the glutathione peroxidase-1 (Gpx-1) knockout mouse brain in response to ischemia/reperfusion injury. J Neurochem. 2001;78:1389–99. https://doi.org/10.1046/j.1471-4159.2001.00535.x.
21. Aibar S, et al. SCENIC: single-cell regulatory network inference and clustering. Nat Methods. 2017;14:1083–6. https://doi.org/10.1038/nmeth.4463.
22. Bringmann A, et al. Müller cells in the healthy and diseased retina. Progress Retinal Eye Res. 2006;25:397–424. https://doi.org/10.1016/j.preteyeres.2006.05.003.
23. Takasaki S, Hayashida K, Morita C, Ishibashi H, Niho Y. CD56 directly interacts in the process of NCAM-positive target cell-killing by NK cells. Cell Biol Int. 2000;24:101–8. https://doi.org/10.1006/cbir.1999.0457.
24. Jiang S, Kametani M, Chen DF. Adaptive immunity: new aspects of pathogenesis underlying neurodegeneration in glaucoma and optic neuropathy. Front Immunol. 2020;11:65. https://doi.org/10.3389/fimmu.2020.00065.
25. Minhas G, Sharma J, Khan N. Cellular stress response and immune signaling in retinal ischemia-reperfusion injury. Front Immunol. 2016;7:444. https://doi.org/10.3389/fimmu.2016.00444.
26. Cai X, et al. Long noncoding RNA Taurine-upregulated gene 1 knockdown protects cardiomyocytes against hypoxia/reoxygenation-induced injury through regulating miR-532–5p/Sox8 Axis. J Cardiovasc Pharmacol. 2020;76:556–63. https://doi.org/10.1097/fjc.0000000000000895.
27. Zhang M, Zhu Y, Wei M, Liu H. Neuroprotective effects of miR-30c on rats with cerebral ischemia/reperfusion injury by targeting SOX9. Pathol Res Pract. 2020;216:153271. https://doi.org/10.1016/j.prp.2020.153271.
28. Wei W, Zhang Y, Li L, Yang J. SOX9 depletion attenuates retinal ganglion cell ferroptosis through blocking ERK/p38 signaling. Tissue Cell. 2024;87:102315. https://doi.org/10.1016/j.tice.2024.102315.
29. Böhm EW, et al. Oxidative stress in the eye and its role in the pathophysiology of ocular diseases. Redox Biol. 2023;68:102967. https://doi.org/10.1016/j.redox.2023.102967.
30. Baudouin C, Kolko M, Melik-Parsadaniantz S, Messmer EM. Inflammation in Glaucoma: from the back to the front of the eye, and beyond. Progress Retinal Eye Res. 2021;83:100916. https://doi.org/10.1016/j.preteyeres.2020.100916.
31. Li Q, Cheng Y, Zhang S, Sun X, Wu J. TRPV4-induced Müller cell gliosis and TNF-α elevation-mediated retinal ganglion cell apoptosis in glaucomatous rats via JAK2/STAT3/NF-κB pathway. J Neuroinflammation. 2021;18:271. https://doi.org/10.1186/s12974-021-02315-8.
32. Li HJ, et al. Inhibition of miRNA-21 promotes retinal ganglion cell survival and visual function by modulating Müller cell gliosis after optic nerve crush. Exp Cell Res. 2019;375:10–9. https://doi.org/10.1016/j.yexcr.2019.01.009.
33. Tian F, et al. Core transcription programs controlling injury-induced neurodegeneration of retinal ganglion cells. Neuron. 2024;112:2453–6. https://doi.org/10.1016/j.neuron.2024.06.009.
34. Hartsock MJ, et al. A mouse model of retinal ischemia-reperfusion injury through elevation of intraocular pressure. J Visualized Exp JoVE. 2016. https://doi.org/10.3791/54065.
35. Palmhof M, et al. From ganglion cell to photoreceptor layer: timeline of deterioration in a rat ischemia/reperfusion model. Front Cell Neurosci. 2019;13:174. https://doi.org/10.3389/fncel.2019.00174.
36. Yao F, et al. Pathologically high intraocular pressure disturbs normal iron homeostasis and leads to retinal ganglion cell ferroptosis in glaucoma. Cell Death Differ. 2023;30:69–81. https://doi.org/10.1038/s41418-022-01046-4.
37. Aredo B, Kumar A, Chen B, Xing C, Ufret-Vincenty RL. Single cell RNA sequencing analysis of mouse retina identifies a subpopulation of Muller glia involved in retinal recovery from injury in the FCD-LIRD model. Invest Ophthalmol Vis Sci. 2023;64:2. https://doi.org/10.1167/iovs.64.11.2.
38. Butler A, Hoffman P, Smibert P, Papalexi E, Satija R. Integrating single-cell transcriptomic data across different conditions, technologies, and species. Nat Biotechnol. 2018;36:411–20. https://doi.org/10.1038/nbt.4096.
39. Hafemeister C, Satija R. Normalization and variance stabilization of single-cell RNA-seq data using regularized negative binomial regression. Genome Biol. 2019;20:296. https://doi.org/10.1186/s13059-019-1874-1.
40. Korsunsky I, et al. Fast, sensitive and accurate integration of single-cell data with Harmony. Nat Methods. 2019;16:1289–96. https://doi.org/10.1038/s41592-019-0619-0.
41. Ianevski A, Giri AK, Aittokallio T. Fully-automated and ultra-fast cell-type identification using specific marker combinations from single-cell transcriptomic data. Nat Commun. 2022;13:1246. https://doi.org/10.1038/s41467-022-28803-w.
42. Jin S, Plikus MV, Nie Q. CellChat for systematic analysis of cell-cell communication from single-cell transcriptomics. Nat Protoc. 2025;20:180–219. https://doi.org/10.1038/s41596-024-01045-4.
43. Baron CS, van Oudenaarden A. Unravelling cellular relationships during development and regeneration using genetic lineage tracing. Nat Rev Mol Cell Biol. 2019;20:753–65. https://doi.org/10.1038/s41580-019-0186-3.
44. Léger H, Santana E, Beltran WA, Luca FC. Preparation of Mouse Retinal Cryosections for Immunohistochemistry. J Visualized Exp JoVE. 2019. https://doi.org/10.3791/59683.
45. Wu X, et al. Spatial multi-omics at subcellular resolution via high-throughput in situ pairwise sequencing. Nat Biomed Eng. 2024;8:872–89. https://doi.org/10.1038/s41551-024-01205-7.

Publisher's Note